

# Journal Pre-proof

Experimental Demonstration of SnO<sub>2</sub> Nanofiber-Based Memristors and Their Data-Driven Modeling for Nanoelectronic Applications

Soumi Saha, Madadi Chetan Kodand Reddy, Tati Sai Nikhil, Kaushik Burugupally, Sanghamitra DebRoy, Akshay Salimath, Venkat Mattela, Surya Shankar Dan, Parikshit Sahatiya

PII: S2709-4723(23)00038-2

DOI: <https://doi.org/10.1016/j.chip.2023.100075>

Reference: CHIP 100075

To appear in: *Chip*

Received Date: 15 June 2023

Revised Date: 10 October 2023

Accepted Date: 14 November 2023

Please cite this article as: Saha S, Kodand Reddy MC, Nikhil TS, Burugupally K, DebRoy S, Salimath A, Mattela V, Dan SS, Sahatiya P, Experimental Demonstration of SnO<sub>2</sub> Nanofiber-Based Memristors and Their Data-Driven Modeling for Nanoelectronic Applications, *Chip*, <https://doi.org/10.1016/j.chip.2023.100075>.

This is a PDF file of an article that has undergone enhancements after acceptance, such as the addition of a cover page and metadata, and formatting for readability, but it is not yet the definitive version of record. This version will undergo additional copyediting, typesetting and review before it is published in its final form, but we are providing this version to give early visibility of the article. Please note that, during the production process, errors may be discovered which could affect the content, and all legal disclaimers that apply to the journal pertain.

© 2023 Published by Elsevier B.V. on behalf of Shanghai Jiao Tong University.



# Experimental Demonstration of SnO<sub>2</sub> Nanofiber-Based Memristors and Their Data-Driven Modeling for Nanoelectronic Applications

Soumi Saha<sup>1</sup>, Madadi Chetan Kodand Reddy<sup>2</sup>, Tati Sai Nikhil<sup>2</sup>, Kaushik Burugupally<sup>2</sup>, Sanghamitra DebRoy<sup>3</sup>, Akshay Salimath<sup>3</sup>, Venkat Mattela<sup>4</sup>, Surya Shankar Dan<sup>1</sup> and Parikshit Sahatiya<sup>1</sup>

<sup>1</sup> Department of Electrical & Electronics Engineering, Birla Institute of Technology and Science Pilani, Hyderabad Campus, 500078 India. (e-mail: parikshit@hyderabad.bits-pilani.ac.in; ssdan@hyderabad.bitspilani.ac.in)

<sup>2</sup> Department of Computer Science and Information Systems, Birla Institute of Technology and Science Pilani, Hyderabad Campus, 500078 India

<sup>3</sup> Nanomagnetic Division, Ceremorphic India Pvt Ltd.

<sup>4</sup> Ceremorphic, Inc., San Jose, California 95131, United States of America

**This paper demonstrates the fabrication, characterization, data-driven modeling, and practical application of a 1D SnO<sub>2</sub> nanofiber-based memristor, in which a 1D SnO<sub>2</sub> active layer is sandwiched between silver (Ag) and aluminum (Al) electrodes. This device yields a very high  $R_{OFF}:R_{ON} \sim 10^4$  ( $I_{ON}:I_{OFF} \sim 10^5$ ) with an excellent activation slope of 10 mV/dec, low set voltage  $V_{SET} \sim 1.14$  V, and good repeatability. This paper physically explains the conduction mechanism in the layered SnO<sub>2</sub> nanofiber-based memristor. The conductive network comprises nanofibers that play a vital role in the memristive action, as more conductive paths could promote the hopping of electron carriers. Energy band structures experimentally extracted using ultraviolet photoelectron spectroscopy (UPS) strongly support the claims reported in this paper. We have developed an ML-assisted, data-driven model of the fabricated memristor using different popular algorithms such as Polynomial Regression, Support Vector Regression (SVR), k Nearest Neighbors (kNN), and Artificial Neural Network (ANN) to model the data of the fabricated device. We have proposed two types of ANN models (type I and type II) algorithms, illustrated with a detailed flowchart, to model the fabricated memristor. Benchmarking with standard ML techniques shows that the type II ANN algorithm provides the best Mean Absolute Percentage Error (MAPE) of 0.0175 with a 98%  $R^2$  score. We have further validated the proposed data-driven model with the characterization results of similar new memristors fabricated using the same fabrication recipe, giving satisfactory predictions. Lastly, we have applied the ANN type II model to design and implement simple AND & OR logic functionalities using the fabricated memristors with expected, near-ideal characteristics.**

**Keywords:** Nanofiber-Based Memristors, Data-driven Modeling, Artificial Neural Network (ANN), SnO<sub>2</sub>

In the present context of fabless manufacturing, semiconductor device models play a critical role in emulating the fabricated device in any application. The traditional compact model development required a vast pool of experimental/simulation data to be manually fitted and optimized with various parameters<sup>1-4</sup>. Furthermore, these models had to be periodically updated with newer device physics, often requiring the development of the same from scratch. Recently, machine learning (ML) tools have gained popularity in various scenarios<sup>5-9</sup>. Also, ML has immense potential to improve the development of any compact model of any semiconductor device<sup>10,11</sup>. In this regard, we have derived the data-driven models from many experimental observations. Owing to its support for a broader range of

regression methods, one can use these ML techniques to develop device models supporting multiple hierarchies. These will further cater to the requirement of the tailored device model suitable for specific circuit or device simulations.

As the memristor fabrication technologies are yet to be standardized, their theoretical models may not consider the various challenges associated with the fabrication of memristors, namely, variability in terms of terminal contacts, packaging, process parameter variations, measuring equipment accuracy, etc., that are usually ignored in the physics-based analytical modeling approach. Thus, one should prefer a data-driven modeling approach using the experimentally characterized data on fabricated devices to incorporate all the practical issues associated with the memristors in the compact model.

Among the various structures of metal-oxide memristors, e.g., nanorods<sup>12–15</sup>, nanobelts<sup>16–19</sup>, nanofibers<sup>20–22</sup>, nanowires<sup>23–27</sup>, etc., nanofiber memristors are suitable for the development of advanced and novel electronic and optoelectronic devices<sup>28</sup>. A large variety of metal oxides, such as  $\text{TiO}_2$ <sup>29</sup>,  $\text{SnO}_2$ ,  $\text{HfO}_2$ ,  $\text{CeO}_2$ , etc., have been well studied for memristive applications. Even though Sn (owing to multiple oxidation states) has a large oxide family ( $\text{SnO}_2$ ,  $\text{Sn}_2\text{O}_3$ ,  $\text{Sn}_3\text{O}_4$ ,  $\text{SnO}$ ), applications of  $\text{SnO}_2$  in memristor are primarily limited due to the high conductance of conventional  $\text{SnO}_2$  thin film. Previous reports on artificial synapse based on a gate tunable, 2 nm thick 2D  $\text{SnO}_2$  memristor gave an  $R_{\text{OFF}}:R_{\text{ON}}$  ratio of  $\sim 10$ , operating within  $\pm 15$  V<sup>30</sup>.  $\text{SnO}_2$  is a well-known n-type semiconductor with superior electron mobility, whose high surface-to-volume ratio of 1D nanofiber  $\text{SnO}_2$  form offers significant deep-level traps. This enhances the memory window, response time, set voltage, and current level of a memristor. To the best of the authors' knowledge, the 1D  $\text{SnO}_2$  memristor has not been reported yet. Furthermore, its data-driven model will open new promising avenues for novel and complex applications.

This paper experimentally demonstrates a 1D  $\text{SnO}_2$  nanofiber-based memristor on a p-type Si substrate for the first time. With the help of the electrospinning technique,  $\text{SnO}_2$  nanofiber with an average diameter of 759.2 nm is deposited. Silver (Ag) and aluminum (Al) are used in the fabricated memristor as the top and bottom electrodes, respectively. The electrospun n-type  $\text{SnO}_2$  nanofiber is used as the active layer of the fabricated memristor. The proposed device exhibits a very high  $R_{\text{OFF}}:R_{\text{ON}} \sim 10^4$  ( $I_{\text{ON}}:I_{\text{OFF}} \sim 10^5$ ) with an excellent activation slope of 10 mV/dec, low set voltage  $\sim 1.14$  V, and good repeatability. The device operation has been explained with the help of device physics. Eventually, a compact data-driven model in conjunction with ML-based techniques of the fabricated memristor is also presented. Different algorithms such as Polynomial Regression, Support Vector Regression (SVR), K Nearest Neighbors (KNN), and Artificial Neural Network (ANN) were used to model the experimental data of the fabricated device. Finally, the proposed two models using ANN techniques were observed to provide the best compact models based on  $R^2$  and *Mean Absolute Percentage Error* (MAPE). Elaborated flowcharts, ANN architectures, data modeling, and model validation are presented in detail in the manuscript.

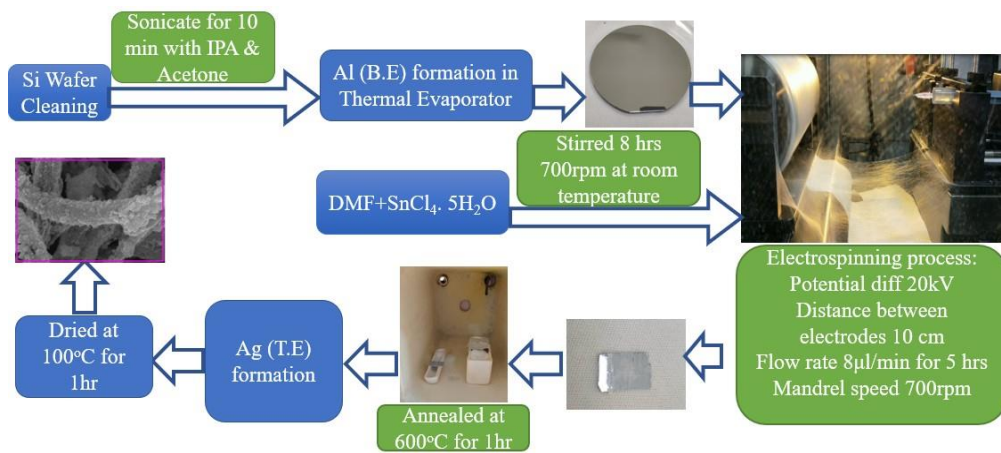


**Fig. 1** | Complete schematic indicating synthesis and device fabrication of the 1D- $\text{SnO}_2$  nanofiber-based memristor.

## RESULTS AND DISCUSSION

**Materials Characterizations.** Fig. 2a depicts the XRD pattern of the pristine SnO<sub>2</sub> nanofibers. A tetragonal rutile structure was confirmed by the attained characteristic peaks with planes (110), (101), (200), (111), (210), (211), (220), (002), (310), (112), (301), (202), and (321) at appropriate diffraction angles<sup>31</sup>. The obtained results corroborate with standard literature (JCPDS-41-1445). Fig. 2b illustrates the XPS survey spectra of synthesized SnO<sub>2</sub> nanofibers, wherein Sn 4d, Sn 3d, O 1s, Sn 3p<sub>3</sub>, and Sn 3p<sub>1</sub> were observed at appropriate binding energies (BE). Fig. 2c depicts the deconvoluted core-level fitted XPS spectra of Sn 3d with two doublet peaks, i.e., Sn 3d<sub>3/2</sub> and Sn 3d<sub>5/2</sub> ascribed to ~495.3 and ~486.88 eV BEs, respectively. Fig. 2d shows the deconvoluted XPS spectra of O 1s with two prominent peaks corresponding to the lattice (O<sub>L</sub>), oxygen vacancies (OV), and adsorbed oxygen species (O<sub>A</sub>) observed at ~530.7, ~532.28 eV, and ~533.08 eV, respectively. Referring to the core-level spectra of O1s, the estimated lattice oxygen, vacancy oxygen, and chemically adsorbed oxygen are 80.2%, 14.5%, and 5.2%, respectively. Evidently, chemically adsorbed oxygen is less compared to available oxygen vacancies, and thus, vacancy indeed plays a significant role in the memristive action. These results indicate that the amount of adsorbed oxygen is increased by introducing SnO<sub>2</sub> nanofiber. Surface-adsorbed oxygen tends to form more active sites, thereby increasing the traps supporting the memristive action. Fig. 2e features the HR-SEM image of the deposited nanofiber in top view on the fabricated device. The mesh will contain several vacant spaces (Fig. 2e), and multiple nanofibers overlayed on each other. The statistical distribution of the measured diameter of the synthesized SnO<sub>2</sub> nanofibers is illustrated in Fig. 2e (inset). Calculation suggests that an average diameter of 762.3 nm is achieved with mean=1.24, median 1.245, and SD=0.09. The roughness of the electrospun nanofiber shown in Fig. 2f is measured using the Scanning Tunneling Microscope (STM). The area can be measured at 200 × 200 nm<sup>2</sup>, and the roughness (in terms of the measured tip currents) is 30 nA to 68 nA. We have repeated the process to cover the 2 × 2 μm<sup>2</sup> area, and the roughness average (R.A.) is found to be 1.8 nA.

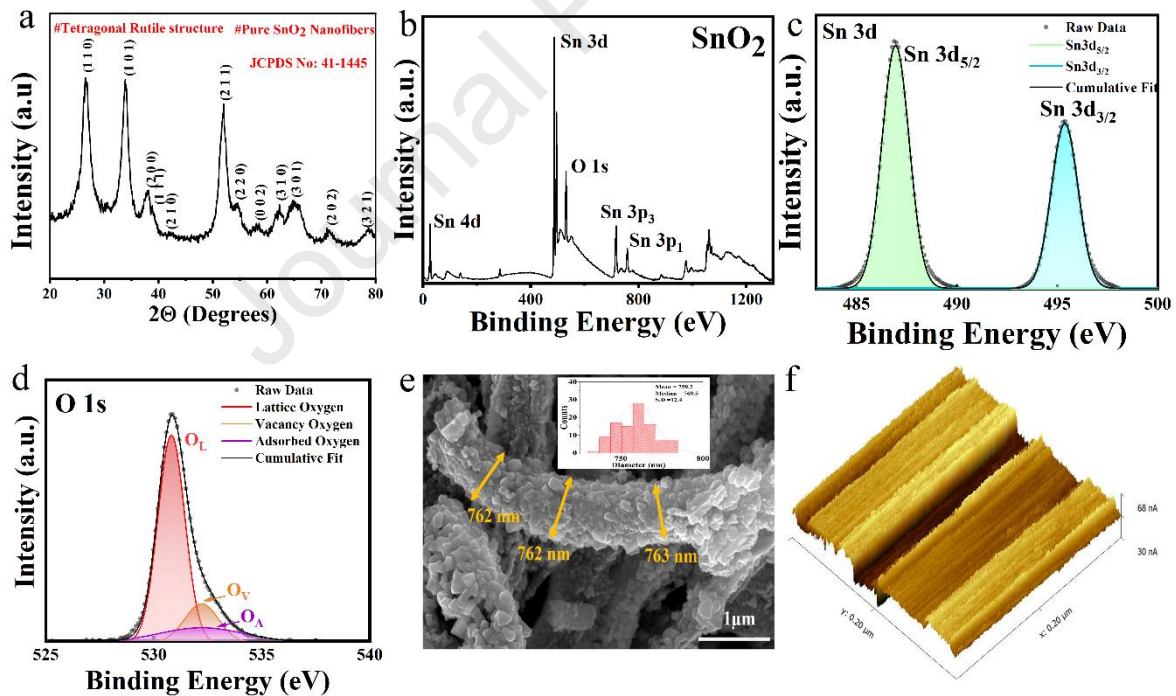


**Fig. 2** **a**, XRD spectrum for pristine SnO<sub>2</sub> nanofiber. **b**, high-resolution XPS survey spectrum of pristine SnO<sub>2</sub> nanofiber. **c**, high-resolution core-level fitted XPS spectra for the elements Sn 3d. **d**, high-resolution core-level fitted XPS spectra for the elements O 1s. **e**, High-resolution FE-SEM images of SnO<sub>2</sub> nanofibers in top view with the statistical distribution of the diameter of the nanofiber (in set) with mean=1.24, median 1.245 and SD=0.09. **f**, Surface roughness of the SnO<sub>2</sub> nanofiber deposited on the Al-coated Si wafer,

**Electrical Characterizations.** Fig. 3a shows the schematic of the proposed device fabricated on the p-type Si wafer. Al (~70 nm) is deposited using the thermal evaporation technique. For the synthesized SnO<sub>2</sub> nanofiber, experimental measurements indicated an average thickness of 762 nm for the individual nanofibers. For the complete nanofiber mesh, the measured thickness was approximately 9.4 μm. However, the mesh contains



several vacant spaces (Fig. 2e), and multiple nanofibers overlaid on each other. As a consequence, the bulk nanofiber attains higher thickness. However, for the memristive action in SnO<sub>2</sub> nanofiber, we employed a metal-semiconductor-metal structure, in which the active SnO<sub>2</sub> layer is covered on top with an Ag electrode. During the top electrode deposition via the thermal evaporation technique, metal ions easily migrate/diffuse/transport through the porous SnO<sub>2</sub>-based nanofiber mesh and reach closer to the bottom electrode. As a result, when the metal-semiconductor-metal structure is formed, the thickness of the active layer will be significantly less than the bulk SnO<sub>2</sub> nanofiber structure. Evidently, the measured average thickness of individual nanofibers in the active layer of the fabricated memristor is 762 nm, which is very less compared to the overall thickness of the SnO<sub>2</sub> nanofiber mesh. Fig. 3b shows the current-voltage (I-V) characteristics in a linear scale obtained using a probe station and a Keithley 2450 source meter. An external bias voltage sweeping between  $\pm 2$  V was applied between the electrodes. The measured threshold voltage of the proposed SnO<sub>2</sub> nanofiber-based memristor is  $\sim 1.14$  V, with a saturation current of 0.14 mA. The fabricated device exhibits the memristor's signature hysteresis. I-V characteristics in the logarithmic scale in Fig. 3c indicate that initially, the memristor operates in a High Resistance State (HRS) when a low DC voltage sweep was applied (0 V to 1.14 V), voltage from 1.14 V to 1.145 V, the measured current showed a sharp increase from  $3.35 \times 10^{-7}$  A (0.335  $\mu$ A) to  $2.76 \times 10^{-5}$  A (27.6  $\mu$ A), demonstrating a switching from the OFF state to the Low Resistance State (LRS) or the ON state. The OFF/ON transformation process could be deemed a 'writing' process in digital storage<sup>32-35</sup>. The current level could be maintained at LRS regardless of applying another positive voltage sweep from 0 to 2 V, a negative voltage sweep from 0 to -2 V, or even removing the power supply, which served as a 'reading' process in digital storage. However, the current declined steadily from -0.55 V to -0.33 V when the device underwent a negative sweep from 0 to -2 V, indicating from the LRS to HRS state. This transition represented that the stored information could be readily erased. Notably, the nanofiber-based device could realize the ON/OFF transformation by switching the positive or negative applied voltage. With the applied bias, the fabricated device started to conduct by forming the conduction filament. The current response shows that the conduction mechanism started at 0.86 V, and the subsequent switching happens at 1.14 V and 1.62 V, respectively. These multiple switching characteristics can be beneficial for applications that require multiple saturation current levels. The availability of multiple oxidation states of Sn can be the probable reason for this phenomenon. The activation slope of the fabricated device is 10 mV/dec with  $R_{OFF}:R_{ON} \sim 10^4$  ( $I_{ON}:I_{OFF} \sim 10^5$ ), clearly visible in Fig. 3c. The pattern is repeated for the consecutive 100-cycle I-V characteristics in Fig. 3d, where we have shown the interval of the 4<sup>th</sup> cycle data for proper observation. For the 1<sup>st</sup> cycle, switching happens at 1.62 V, and switching happens for the 100<sup>th</sup> cycle at 0.92 V. The SET voltage  $V_{SET}$  of the consecutive cycles (like for the 4<sup>th</sup>, 8<sup>th</sup>, and so on) decreases with the presence of the localized ions, and beyond that, it remains almost the same. The I-V response for 100 consecutive cycles shows very stable switching from high resistance (HRS) to low (LRS) and vice versa. The multiple switching characteristics are also present in these plots. HRS signifies the data writing, LRS signifies the data memorization or holding the data, and the breakdown voltage  $V_{BR}$  signifies the data erase. These three characterize the properties of the memristor. The variation of  $V_{BR}$  for 100 consecutive cycles from -0.61 V to -0.33 V is also visible in Fig 3d. Fig 3e depicts the fabricated memristor's current HRS and LRS currents for 1000 consecutive cycles. The result indicates that  $R_{OFF}:R_{ON} \sim 10^4$  ( $I_{ON}:I_{OFF} \sim 10^5$ ) does not alter significantly with the cycle number (except for the first cycle). The average current values of HRS and LRS are  $\sim 1$  nA and 0.1 mA, respectively. Fig. 3f depicts the statistical variation in measured  $V_{SET}$  for 30 switching cycles, confirming the stability of the device. The mean value of  $V_{SET}$  is approximately 1.24 V.

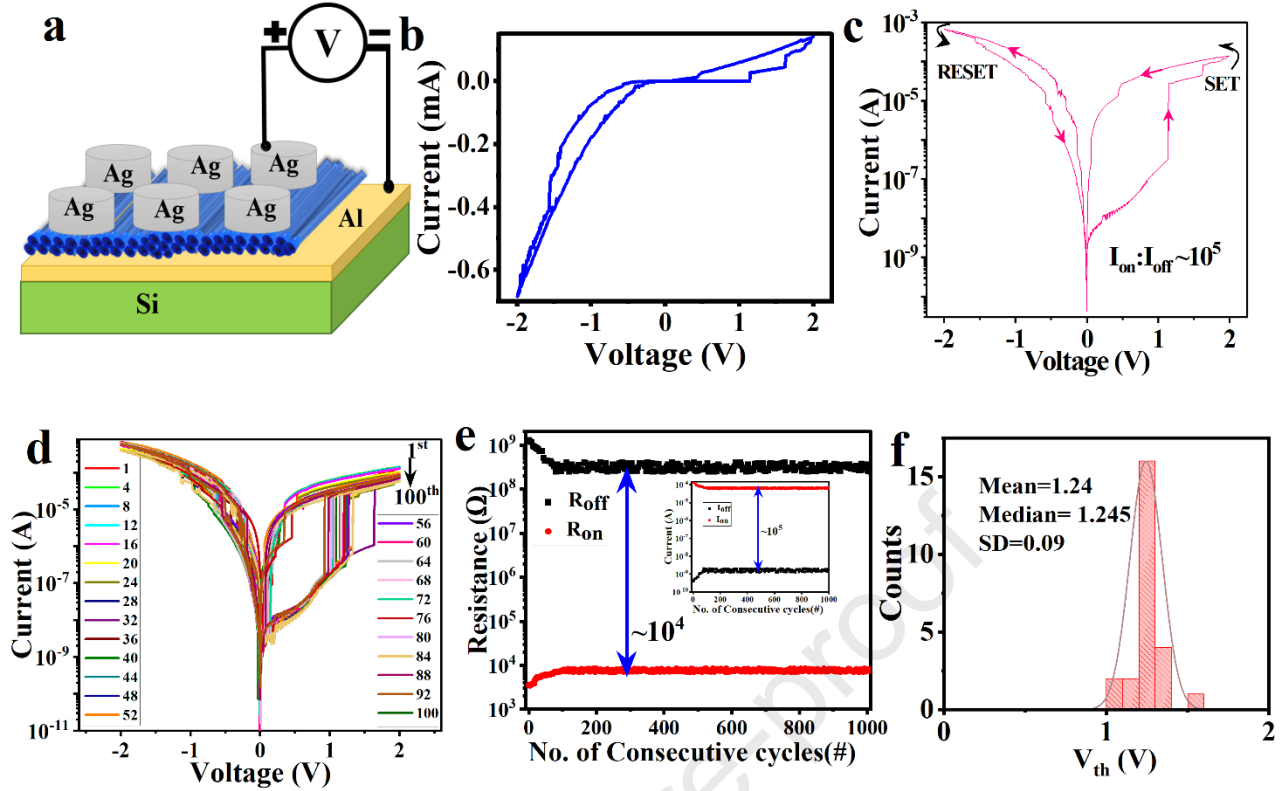


**Fig. 3** | **a**, Schematic of the fabricated 1D SnO<sub>2</sub> nanofiber-based memristor. **b**, Measured I-V characteristics of the fabricated memristor in linear at room temperature. **c**, Measured I-V characteristics of the fabricated memristor in logarithmic scales at room temperature. **d**, I-V characteristics in logarithmic scale for 100 consecutive cycles. **e**, variation of R<sub>ON</sub> and R<sub>OFF</sub> for 1000 consecutive switching cycles with a variation of I<sub>ON</sub> and I<sub>OFF</sub> for 1000 consecutive switching cycles inset. **f**, the statistical distribution of the V<sub>SET</sub> for 30 switching cycles.

**Conduction Mechanism.** The conduction mechanism of the fabricated memristor can be explained using the schematic of the nanofiber shown in Fig. 4a. The conductive network comprised of nanofibers plays a vital role in the memristive action as more conductive paths would promote exciting hopping of electron carriers. Meanwhile, SnO<sub>2</sub> nanofibers can also provide direct pathways for charge transport<sup>36</sup>. With the help of oxygen vacancies, nanofibers can thus provide direct pathways for charge Ag<sup>+</sup> ions to transport with the applied positive bias. Overlap of the n-type of SnO<sub>2</sub> nanofibers can promote exciting electron carriers through the hopping mechanism. The migration of Ag<sup>+</sup> ions is a vertical migration. As depicted in the FE-SEM image in Fig 4a (inset) of the fabricated nanofibers, there are finite gaps between the synthesized nanofibers. When the top electrode is deposited via thermal evaporation, metal ions are also deposited on the bottom nanofiber layer owing to its porous structure. Therefore, the actual metal-semiconductor-metal structure exhibiting the signature memristive characteristics consists of a monolayer or few layers of SnO<sub>2</sub> nanofibers. Thus, during the forming process, the Ag<sup>+</sup> ions migrate vertically along the nanofiber, and a conduction bridge is formed at the appropriate bias level. The energy band diagram and the Ultraviolet Photoelectron Spectroscopy (UPS) spectra, along with UV-Vis absorption spectra and Tauc plot (inset) of synthesized SnO<sub>2</sub> nanofiber are shown in Fig. 4b inset. A UV-Vis absorption study was conducted to estimate the bandgap, and then the Tauc plot shown in Fig 4b inset to estimate the bandgap of synthesized SnO<sub>2</sub> nanofiber, which was measured to be ~ 2.25 eV. From the UPS study, the Fermi edge (E<sub>F</sub>) of 1.36 eV and E<sub>homo</sub> of 1.57 eV are derived, and the work function (Φ) is calculated (Equation 1) of 4.63 eV. With this information, we have drawn the energy band diagram of the SnO<sub>2</sub>.

$$\Phi = h\nu - E_{\text{cut-off}} - E_F = 4.63 \text{ eV} \quad (1)^{37}$$

Where  $h\nu$  represents the energy of the He-I source (i.e., 21.22 eV),  $E_{\text{cut-off}}$  is the binding energy at the higher energy end of the spectrum, i.e., 15.23 eV. The work function of the SnO<sub>2</sub> nanofiber is then calculated as 4.63 eV, and the work function value of Ag is 4.7 eV<sup>38</sup>, adopted from the literature. The vacuum levels of SnO<sub>2</sub> and Ag in standalone/bulk conditions will have equal vacuum levels, represented in Fig 4c. However, a

Schottky barrier will form between the semiconductor ( $\text{SnO}_2$ ) and the metal electrode (Ag), leading to the band bending at the interface shown in Fig 4d. This bending will also cause a bending of the vacuum level. The 0.1 eV difference in the work function of  $\text{SnO}_2$  and Ag helps the device to start the conduction mechanism at a lower voltage (i.e., 0.66 V). The I-V characteristics Fig. 3c indicate that the conduction bridge was completely formed around 1.14 V. Beyond 1.14 V, the current increases sharply.

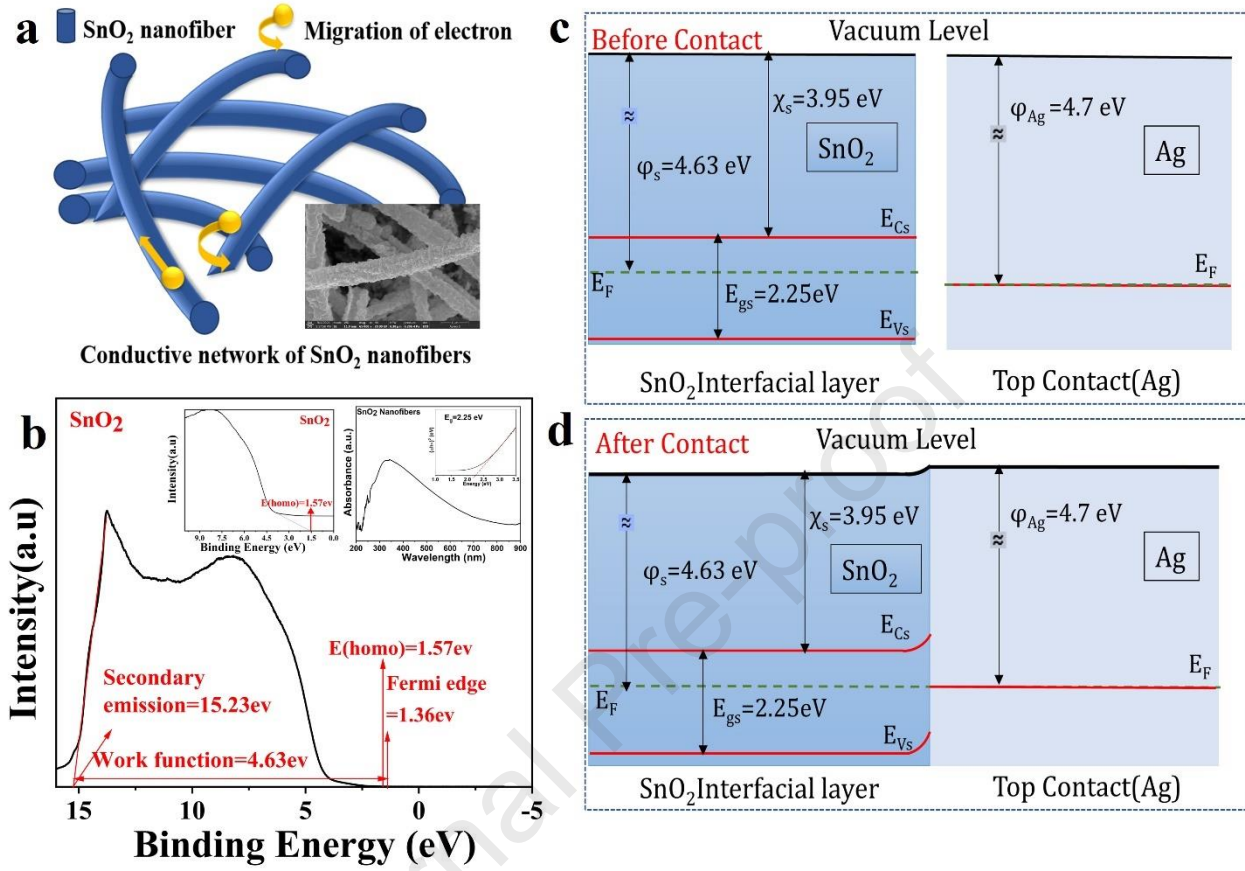


**Fig. 4** | **a**, Schematic diagram of conduction mechanism of  $\text{SnO}_2$  nanofibers with high-resolution FESEM images of the  $\text{SnO}_2$  nanofiber in the top view (in set). **b**, Measured UPS spectra of synthesized 1D  $\text{SnO}_2$  with UV-Vis absorption spectra with Tauc plot in the inset. **c-d**, Band structure of the fabricated memristor before contact and after contact. Results of UPS survey spectra of the active material were incorporated to draw the E-B diagram of the fabricated memristor.

## DATA-DRIVEN MODELING

We carried out the data preprocessing on two features. We measured current  $I$  and sequential order no. of measurement cycles (out of a total of 100 cycles, corresponding to  $1.6 \times 10^5$  data points) as functions of the applied bias  $V$ , the independent variable. The sequential order number of the measurement cycles is correlated to the endurance of the fabricated devices. The external bias voltage was swept from  $0 \text{ V} \rightarrow +2 \text{ V} \rightarrow -2 \text{ V} \rightarrow 0 \text{ V}$ . The created datasets were split into two parts: (a) upsweep data and (b) downsweep data. Two different ANN models based on voltage sweeping were developed for each data set, i.e., upsweep and downsweep. However, it should be noted that the different normalization processes applied for the type I model for preprocessing the data in both sweeps are different. In the type I model, the ANN was trained using normalized voltage and normalized cycle number as input features and normalized current as output, keeping the measured current completely hidden. Thus, the output variable in the type I model will be the normalized current on a linear scale.

In the type II model, raw voltage and cycle numbers were used as the input features. Meanwhile, the logarithmic transformation was applied to the current, which was used as the output feature for the training of the ANN algorithm. This was done to increase the efficacy of the derived model to capture important features of the fabricated memristor in the lower range of the measured current. Fig 5 shows the

algorithmic flowchart for the ANN-based modeling.

The ANN architecture used for each of our models is shown in Fig 6. For type I ANN and type II ANN, the output layer has only one node corresponding to the desired output by the proposed model. Additionally, all hidden layers have been scaled down by a factor of 20 to enhance interpretability. We have used the Rectified Linear Unit (ReLU) activation function in the input and hidden layers and a linear activation function in the output layer, which is common in ANN regressions. The loss function for the model is a mean squared error (MSE), and the optimizer used is Adam. The optimization algorithm computes the loss function's gradient and adapts each weight's learning rate during training. To prevent overfitting, we implemented an early stopping callback function with a minimum improvement parameter of 0.0005 for type I and 0.005 for type II and patience (indicates the wait time for the minimum improvement prior to the stop of training) of 50 epochs.

Additionally, we activated the 'restore best weights' option in the early stopping callback. This option enables us to store the best model found during training. We trained the model with a batch size of 10 and 150 epochs.

In the ANN models, we have used a 72:18:10 train-test-validation split, as shown in Table 1.

Table 1 Data splitting among train-test-validation

Dataset	Train	Validation	Test
Size (in %)	72	18	10

It is important to note that the standardization in the case of the type I model shown in Fig. 7 was achieved by scaling the dataset to unit variance and with zero means. Similarly, in the type II model, the ANN algorithm was trained using the original voltage cycle numbers, and the output that the model would be predicting is the current represented on a 10-base logarithmic. In the type II model, as shown in Fig 8, the logarithmic transformation was applied to the device current values before the ANN algorithm training to increase the derived model's efficacy to capture important features of the fabricated memristor in the lower range of current. This was especially done to achieve the key features like the set voltage, abrupt jump in the measure device current, etc., which is common in fabricated memristors while switching from HRS to LRS. The logarithmic transformation was categorically chosen to exploit its steeper slope for lower values of current (I), leading to enhanced disparities between the low values of I. We have also trained another ANN model using untransformed data (raw voltage and cycle numbers as model inputs with current as the model output), which led to a model incapable of exhibiting key features of the memristor, as mentioned earlier. However, with the application of logarithmic transformation on the measured data, the created dataset also had a relatively smaller rescaling for the larger values of I. This led to an underprediction of measured values of I via the ANN model. As such type I model fits the entire data with equal weightage, leading to better performance in metrics like  $R^2$  and MSE.

However, allotting higher priority to lower values of I, which was done in the type II model, is very important to observe key characteristics of the memristor. This behavior of the type II model leads to its better performance in the metric MAPE. A flow chart indicating the various steps of the development of the two data-driven models of the memristor is shown in Fig. 5. We also measured the various fitting parameters of both models. For the type I model, the measured values of  $R^2$  score, mean-squared error (MSE), and MAPE were 0.9985,  $4.2711 \times 10^{-11}$ , and 25.4675, respectively. Similarly, the  $R^2$  score, MSE, and MAPE values for the type II model were found to be 0.9818, 0.0386, and 0.0175, respectively.



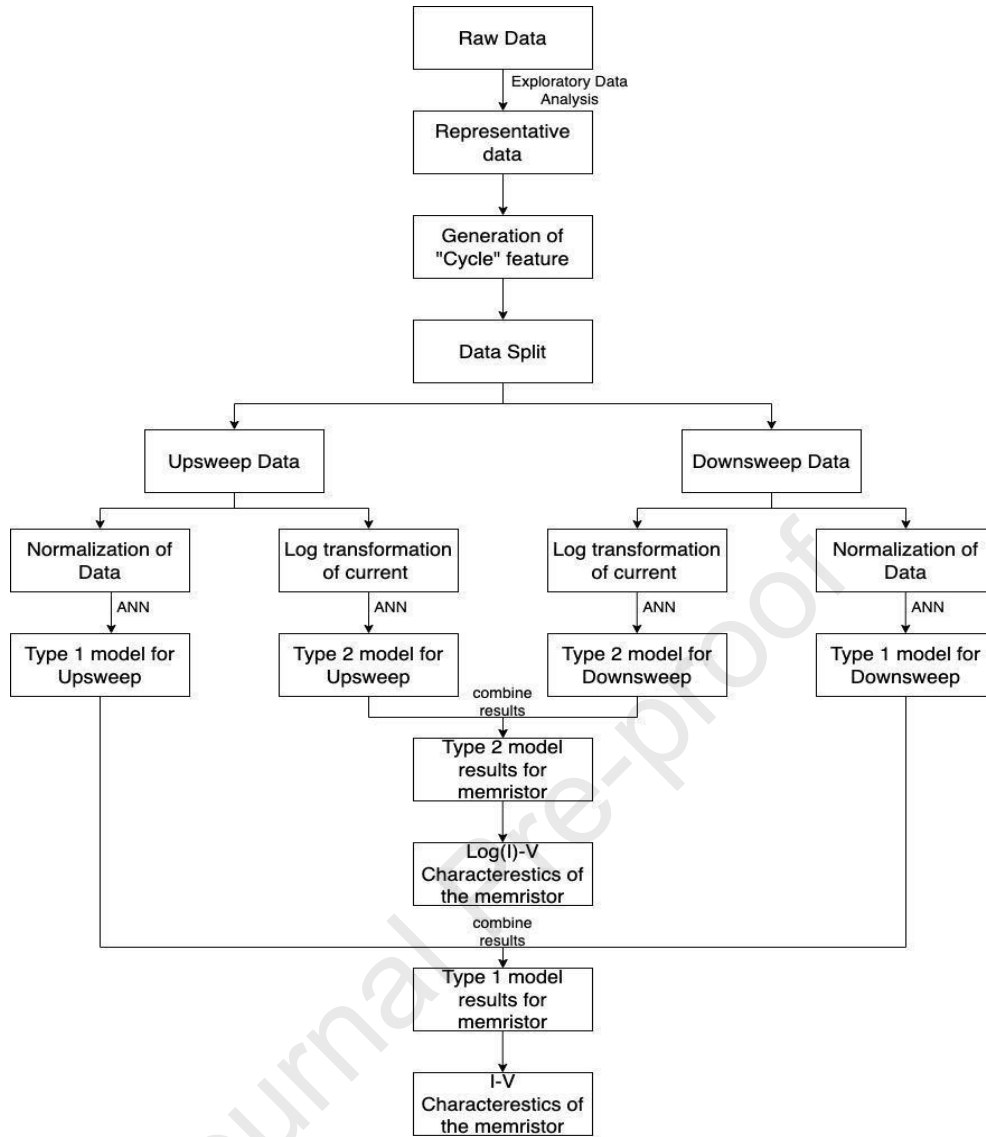


**Fig. 5** | The flow chart indicating the various steps involved in the development of two data drive models of the memristor

In the data-driven modeling of memristors, the coefficient of determination or  $R^2$  is an important metric to evaluate the model's performance.  $R^2$  measures the proportion of the variance in the dependent variable (memristor behavior in this case) explained by the independent variables (features used in the model). A high  $R^2$  value indicates that the model can accurately capture the relationship between the variables, which is crucial in accurately predicting the behavior of memristors. Therefore,  $R^2$  can help researchers determine the efficacy of their data-driven modeling techniques in capturing the behavior of memristors and improving their design.

On the other hand, Mean Absolute Percentage Error (MAPE) is an essential metric in the data-driven modeling of memristors because it measures the percentage of the average absolute error between the measured and predicted values of memristor behavior. MAPE helps to quantify the accuracy of the predictions made by the model. It is particularly useful when dealing with datasets where a small error percentage can significantly impact the model's overall performance. Therefore, MAPE can provide insights into the accuracy and precision of the data-driven model and help researchers identify improvement areas. To find out if our proposed models work well, we benchmarked our models with three other ML models on the 2 metrics-  $R^2$  and MAPE.

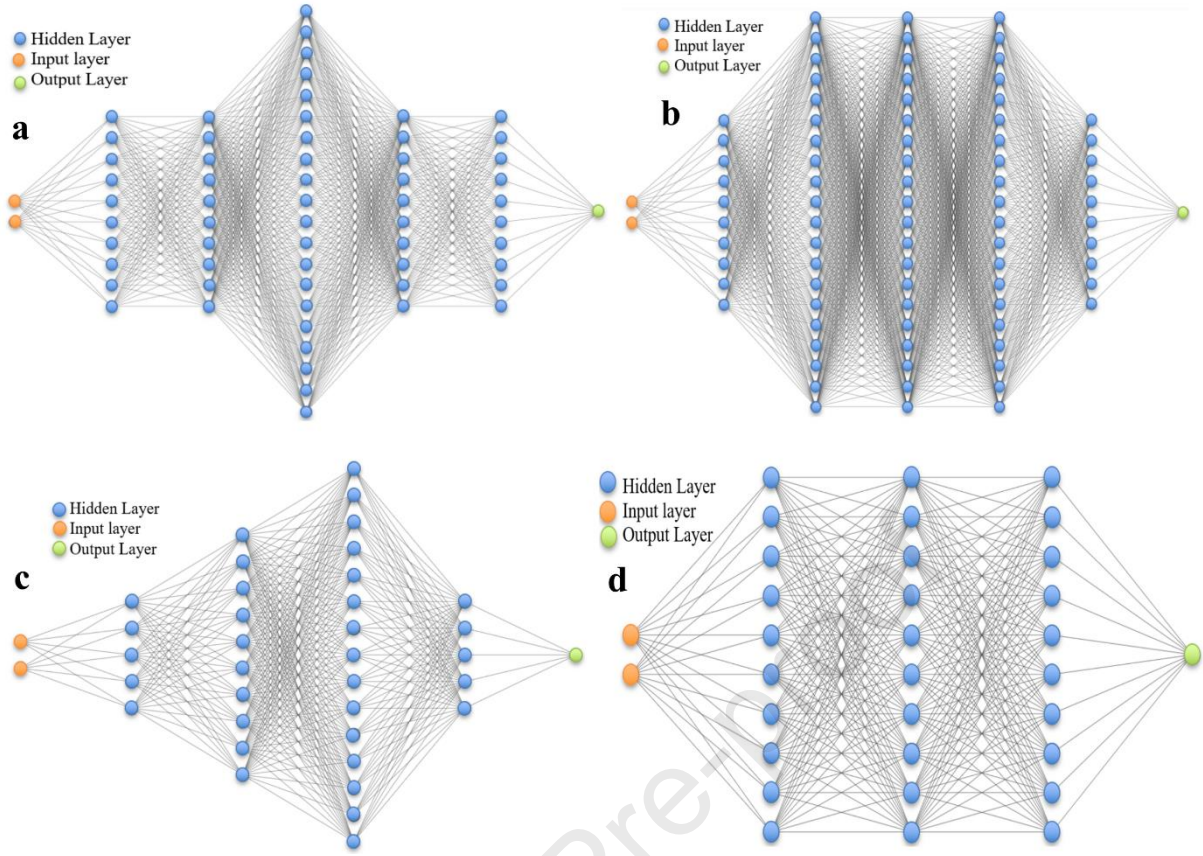


**Fig. 6 | ANN architecture with the input layer, hidden layers have been downsized by a factor of 20 for the above image. a, type I Upsweep. b, type I downsweep. c, type II upsweep. d, type II downsweep.**

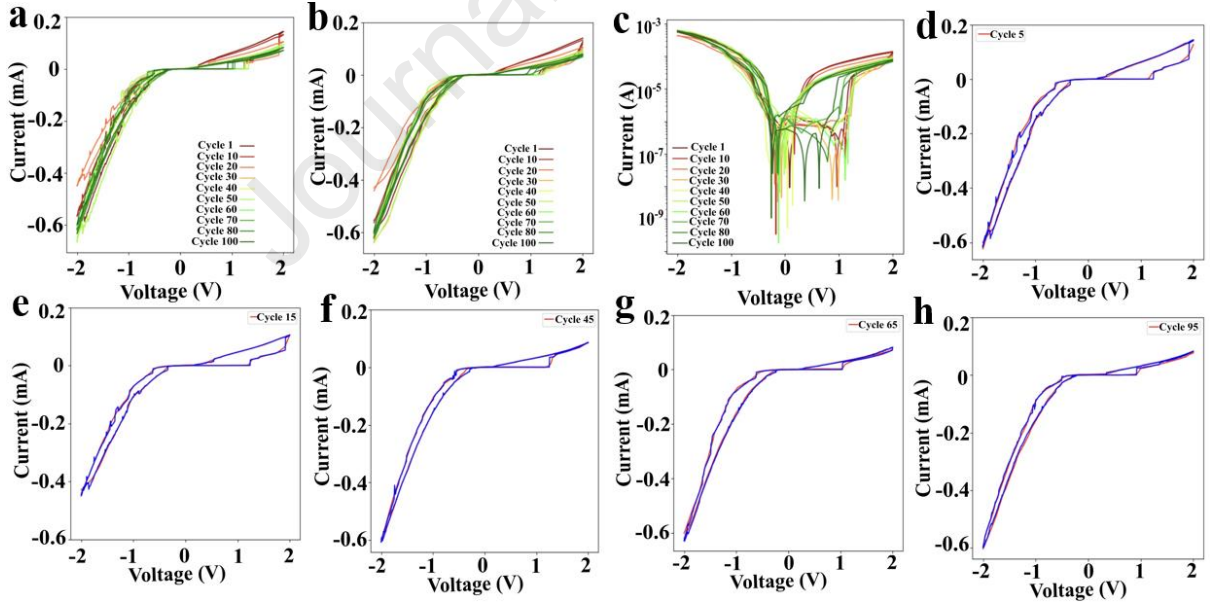


**Fig. 7 | Comparative I-V response for experimental and Type I ANN modeling. a, Measured current I vs. applied voltage V. b, Model output I vs. V with  $R^2=0.9984$ ,  $MSE=4.6802 \times 10^{-11}$  MAPE= 25.4675. c, Model output on the  $\log_{10}$  scale. d-h, Single-cycle comparisons (Blue is for measured data, and Red is the predicted data) for arbitrarily chosen cycle numbers 5, 15, 45, 65, and 95.**

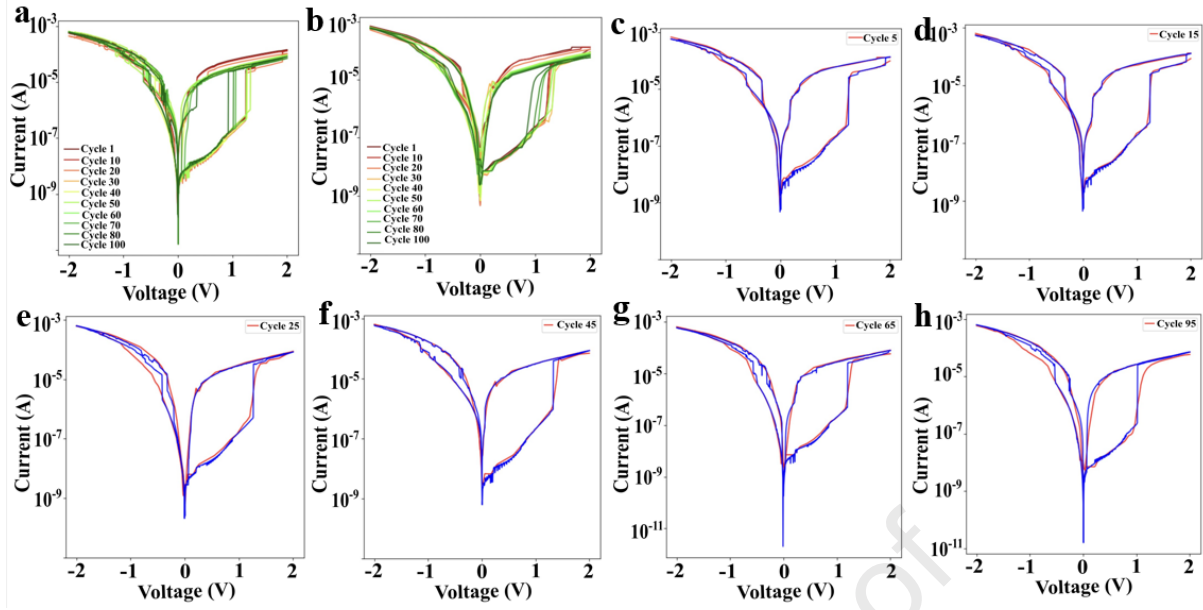


**Fig 8 | Comparative I-V response for experimental and Type II ANN modeling.** **a**, Measured I vs. applied voltage V on the  $\log_{10}$  scale. **b**, Model output I vs. V on the  $\log_{10}$  scale;  $R^2=0.9818$ ,  $MSE=0.0386$ ,  $MAPE=0.0175$ . **c-h**, Single-cycle comparisons-(Blue is for the measured data, and Red is the predicted data) for arbitrarily chosen cycle numbers 5, 15, 25, 45, 65, and 95.

The five models taken for comparative analysis are:

- 1) Polynomial Regression (with Hybrid modeling, i.e., with separate models for high voltage and low voltage where the memristor behaves differently)
- 2) Support Vector Regression
- 3) K Nearest Neighbors
- 4) Type I ANN model
- 5) Type II ANN model

Type II ANN Model had the best MAPE score, indicating that it is the best model for seeing Table 2. Although the KNN model had the best  $R^2$  score and a decent MAPE score, it has the drawback that we cannot use it to predict output for voltage and cycle values not covered by the range of our training data. As such, the type I ANN model, with the second-best  $R^2$  score, is the best model, as seen in Table 2.

Table 2. Performance Evaluation of the different ML-based models for the Fabricated nanofiber based memristor

	Polynomial Regression (with Hybrid modeling)	SVR	KNN (K=5)	Type I ANN	Type II ANN
$R^2$	0.9815	0.9860	0.9997	0.9985	0.9818
MAPE	33.0819	158.9226	0.1257	25.4675	0.0175

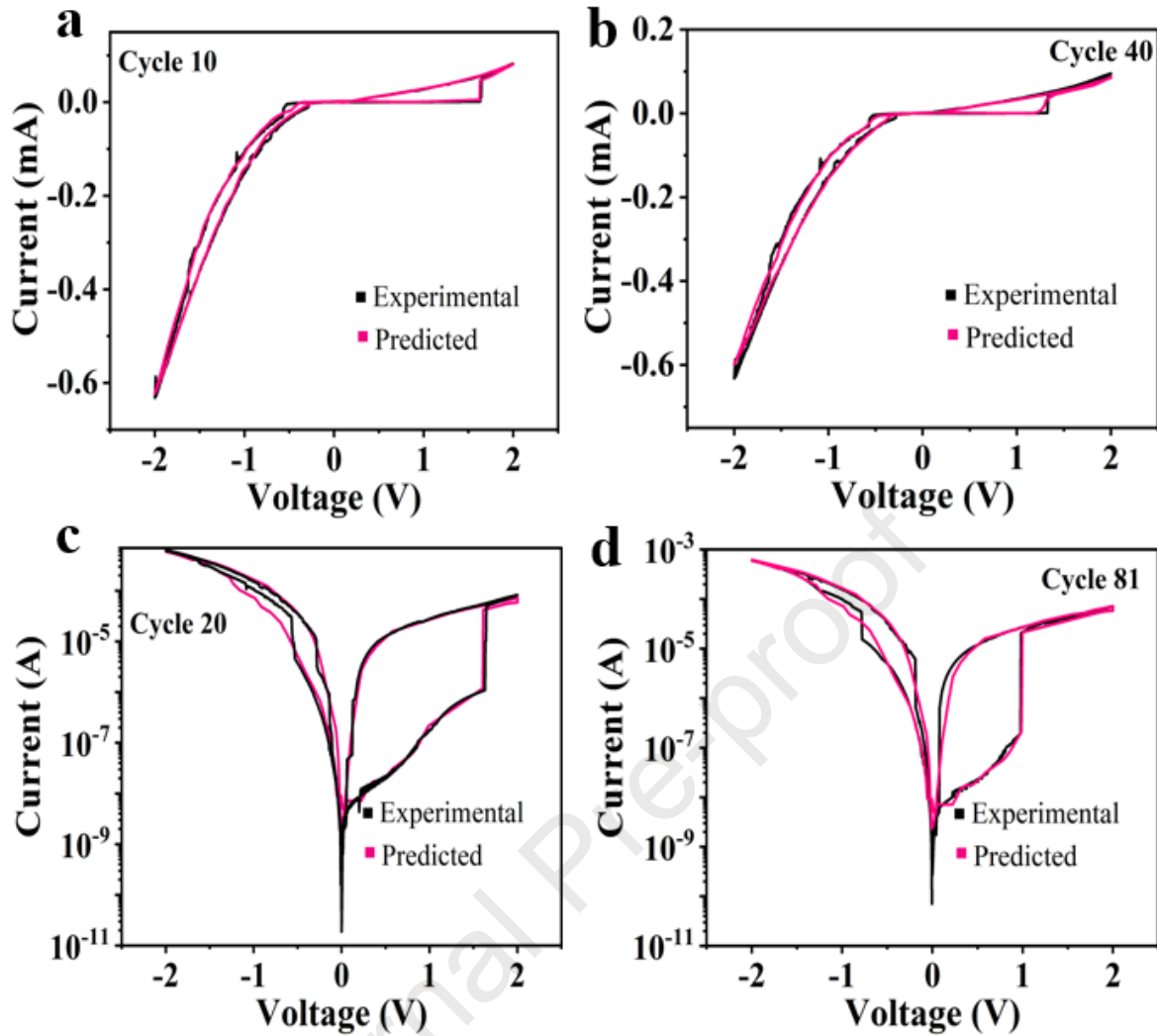


**Fig 9** | **a-b**, the model output (pink) and the experimental output (black) of random cycle data of a newly fabricated device type I ANN for cycle 10 and cycle 40. **c-d**, the model output (pink) and the experimental output (black) of random cycle data of a newly fabricated device type II ANN for cycle 20 and cycle 81.

The best way to validate the model is to test it with the measured data of the new SnO<sub>2</sub> nanofiber-based memristors fabricated using the same process recipe. We have thoroughly checked all 100 cycle data with the modeled data to justify the proposed ANN model's validation. The reliability of type I and type II models are also checked with the same cycle number experimental data of the newly fabricated device in Figs. 9 a-d shows the model works fine with the same fabricated devices. It can be observed that the nonlinearity of the device, the threshold voltage, trend of high and low resistive paths also followed perfectly w.r.to cycle number. As it has been noticed that the threshold voltage decreases with the increasing number of cycles, this exact nature was observed in the new devices as well.

This work was also compared with recently reported fabricated nanofiber-based memristor in terms of active material, a top and bottom electrode, switching window, fabrication technique, and modeling in Table 3. To the best of the authors' knowledge, very few reports are found to provide the best performance and cover data-driven modeling.

Table 3. Performance Evaluation of the Fabricated nanofiber-based memristor

Year	Active material	TE	BE	Switching window	Technique	Modeling	ref
2013	Nb <sub>2</sub> O <sub>5</sub>	DLC	Pt	$2 \times 10^4$	Electrospinning	Thermodyn	<sup>39</sup>



					ning	amic model	
2019	CuO	Al	Cu	50	Spin-Coating	NA	<sup>40</sup>
2020	fMWCNTs-TiO <sub>2</sub>	Ag	FTO	>10	Electrospinning	Space charge limited current model	<sup>41</sup>
2022	LiF	Al	ITO	10 <sup>4</sup>	Electrophoretic-induced self-assembly deposition	Space charge limited current model	<sup>21</sup>
2023	Sericin	Ag	W	>100	Electrospinning	NA	<sup>42</sup>
2023	TiO <sub>2</sub>	SnS/TiO <sub>2</sub>	Ti	10 <sup>2</sup>	Hydrothermal	Physics-Based	<sup>43</sup>
2023	SnO <sub>2</sub> nanofiber	Ag	Al	10 <sup>5</sup>	Electrospinning	Data-driven modeling	<b>This work</b>

#### APPLICATION OF THE DATA-DRIVEN MODEL

When the memristors are connected in the topologies shown in Fig. 10, the outputs X and Y yield the AND and OR functionalities with a caveat. When both A and B are logic high (logic state 1 or logic level  $V_{DD}$ ), nodes X and Y will eventually reach 1 through the charges pumped into the load capacitor  $C_L$  from the  $V_{DD}$  power supplies at A and B. Similarly, when both A and B are logic low (logic state 0 or logic level Gnd), nodes X and Y will eventually reach 0, as  $C_L$  will discharge through the memristors, irrespective of whether the memristors are in their HRS or LRS states. Unlike the typical MOS technology, when one of the inputs is high and the other one low, the robustness of the voltage levels at nodes X and Y will depend on the  $R_{LOW}/R_{HIGH}$  ratios given by  $V_X = \lim_{\frac{R_{LOW}}{R_{HIGH}} \rightarrow 0} V_{DD} \left( \frac{R_{LOW}}{R_{LOW} + R_{HIGH}} \right) = 0$  and  $V_Y = \lim_{\frac{R_{LOW}}{R_{HIGH}} \rightarrow 0} V_{DD} \left( \frac{R_{HIGH}}{R_{LOW} + R_{HIGH}} \right) = V_{DD}$

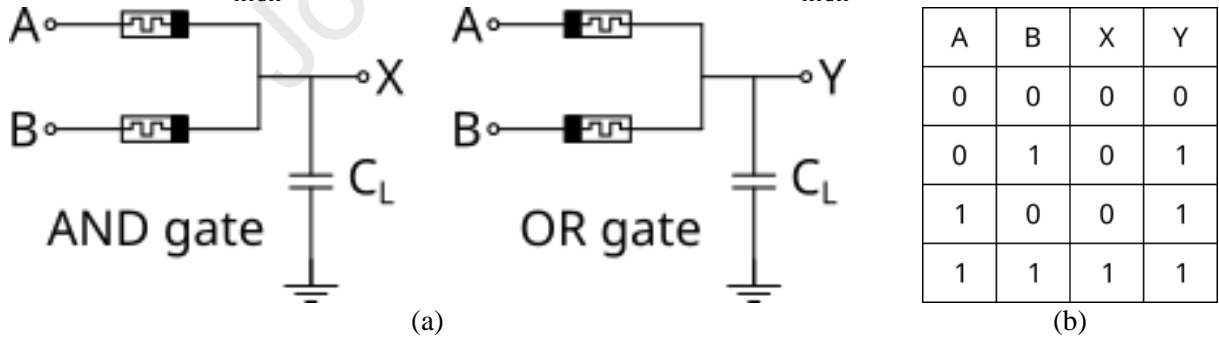


**Fig 10| a**, AND & OR logic implementations using memristors and the **b**, associated truth tables.

Fig. 11(a) shows the ANN type II model of the fabricated SnO<sub>2</sub> memristor's I-V characteristics (Fig. 9) plotted on the linear scale between 0 to 2 V variation corresponding to Gnd and  $V_{DD}$  transition. The inverse gradient of the I-V relation in Fig. 11(a) gives the resistance of the memristor as a function of the applied bias, as predicted by the ANN model. As a benchmarking example, we have chosen the best-case scenario for the circuit design (Fig. 10) by selecting the lowest  $R_{LOW}/R_{HIGH}$  ratio, commensurate with the previous circuit analysis. The ANN model predicted the maximum resistance during the upswing as  $R_{HIGH} = 1105003.204422092\Omega \approx 1.1M\Omega$  and the minimum resistance during the downswing as  $R_{LOW} = 9.107973325443396\Omega \approx 9.1\Omega$ , which makes  $R_{LOW}/R_{HIGH} = 8.242485894153397 \times 10^{-6}$  a good approximation for  $R_{LOW}/R_{HIGH} \rightarrow 0$ .

The inputs A and B in Fig. 11(b) are taken as ideal square pulse trains with 50% duty cycle, 2 V (0 to peak) amplitude, and 0.8  $\mu$ s and 0.4  $\mu$ s time periods (frequencies of 1.25 & 2.5 MHz, respectively). Under no-load condition (i.e.,  $C_L = 0$ ), the output signals X and Y are shown to realize a perfect AND and OR logic implemented using our fabricated memristors. It is worthy of note that such an implementation is far simpler and cheaper than the conventional AND and OR digital ICs available in the market.

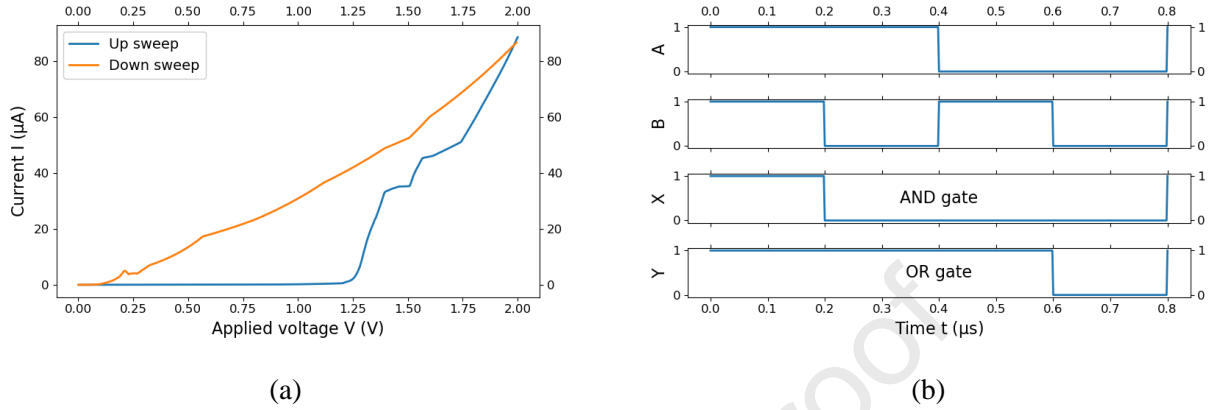


**Fig. 11.** (a) The I-V characteristics predicted by the ANN type II model of the fabricated SnO<sub>2</sub> memristor on a linear scale between 0 and 2 V sweep. (b) The realization of AND and OR logic functionalities using the resistances extracted from the ANN predicted characteristics in (a).

## CONCLUSION

In conclusion, this article successfully demonstrated the fabrication, characterization, and data-driven modeling of the SnO<sub>2</sub> nanofiber-based memristor. The proposed device results in a very high  $R_{OFF}:R_{ON} \sim 10^4$  ( $I_{ON}:I_{OFF} \sim 10^5$ ) with an excellent activation slope of 10 mV/dec, low set voltage  $\sim 1.14$  V, with good repeatability. The switching mechanism is explained by analyzing the derived energy band diagram from the experimental UPS spectra. This article further demonstrates that data-driven modeling uses the memristor's experimental data. With the help of a benchmarking comparison with multiple standard ML algorithms, we have conclusively shown that the type II ANN technique provides the best results based on  $R^2$  scores (98%) and MAPE of 0.0175. The proposed model is further validated with the measured characteristics of new memristor devices fabricated using the same fabrication recipes, and the predictions of our proposed data-driven model match the measured characteristics satisfactorily. Furthermore, the realization of the AND and OR logic using just two memristors provide the same functionality of equivalent CMOS AND and OR logic gate ICs available in the market at a much simpler and cheaper process.

## METHODS

**Materials and instruments.** Polyacrylonitrile (PAN, molecular weight  $\sim 150,000$ ), dimethyl formamide (DMF), and tin chloride ( $\text{SnCl}_4 \cdot 5\text{H}_2\text{O}$ ) were procured from Sigma Aldrich. Deionized water from a Merck Millipore system (resistivity  $\sim 18.2 \text{ M}\Omega \cdot \text{cm}$ ) was utilized for the whole experiment. Without further purification, the chemicals procured were used to synthesize pristine SnO<sub>2</sub> nanofibers using the electrospinning technique. The Field Emission Scanning Electron Microscopy (FESEM) images were obtained using an FEI, LoVac Apreo electron microscope. LoVac X'pert PRO X-Ray Diffraction (XRD) was utilized to know the structural characterization of SnO<sub>2</sub> nanofibers. A Thermo Scientific K- $\alpha$  X-ray Photoelectron Spectroscopy (XPS) instrument was employed to identify the chemical composition and oxidation states of SnO<sub>2</sub> nanofibers. All the electrical characterizations related to memristive properties were performed using a Keithley 2450 source meter and a probe station.

**Synthesis of SnO<sub>2</sub> Nanofibers.** SnO<sub>2</sub> nanofibers were synthesized by utilizing the electrospinning

technique. In brief, PAN (10 wt %) and  $\text{SnCl}_4 \cdot 5\text{H}_2\text{O}$  (4 wt %) were added to DMF solvent, and then, the mixture was stirred for 4 h at room temperature with 750 rpm stirring speed to attain the homogeneous viscous solution that was ready for electrospinning. The electrospinning setup utilized to synthesize nanofibers comprised a high-voltage supply, syringe, needle, and grounded collector.  $\text{SnO}_2$  nanofibers were electrospun on a fixed target with a single side-masked Si wafer coated with Al at room temperature. The fixed target plate with Al coated Si wafer was placed at a distance of 10 cm away from the tip of a 24-gauge needle. Furthermore, continuous deposition of  $\text{SnO}_2$  nanofibers was done on the target for 30 min at 20 kV applied voltage between the needle and the grounded collector with a constant flow rate of 10  $\mu\text{L}/\text{min}$  to obtain a considerable amount of nanofibers on the masked Si wafer. After removal of the mask from the device, the attained  $\text{SnO}_2$  nanofibers were annealed at 600°C for 1 h using a box furnace to eliminate the polymer and unwanted residues in the resultant nanofibers.

**Device Fabrication.** The memristor was fabricated on a <100> p-type Silicon substrate. At first, the Si wafer was thoroughly cleaned using Isopropyl Alcohol (IPA) and acetone and then dried at 100°C for 20 minutes in a high-temperature oven. Subsequently, utilizing the thermal evaporation technique, Al was deposited on Si using a mask that protects the bottom electrodes from electrospinning. Next,  $\text{SnO}_2$  nanofibers were deposited on Al coated Si wafer. After annealing at 600°C for 1h, Ag contacts were made using silver paste. The bottom contact was taken from the Al layer, and the top contact was taken from Ag. The fabricated device dried in a hot air oven at 100 °C for 30 min. The complete schematic for the synthesis and device fabrication of the  $\text{SnO}_2$  nanofiber-based memristor is schematically illustrated in Fig. 1.

## DECLARATION

The authors declare that they have no known competing financial interests or personal relationships that could have appeared to influence the work reported in this paper.

## REFERENCES

1. Nigam, K., McCallum, A. K., Thrun, S. & Mitchell, T. Text Classification from Labeled and Unlabeled Documents using EM. *Mach. Learn.* **39**, 103–134 (2000).
2. Yuan, G. *et al.* An Ultra-Efficient Memristor-Based DNN Framework with Structured Weight Pruning and Quantization Using ADMM. in *2019 IEEE/ACM International Symposium on Low Power Electronics and Design (ISLPED)* 1–6 (2019). doi:10.1109/ISLPED.2019.8824944.
3. The Future of Memristors: Materials Engineering and Neural Networks - Sun - 2021 - Advanced Functional Materials - Wiley Online Library.  
<https://onlinelibrary.wiley.com/doi/full/10.1002/adfm.202006773>.
4. Ran, H., Wen, S., Shi, K. & Huang, T. Stable and compact design of Memristive GoogLeNet Neural Network. *Neurocomputing* **441**, 52–63 (2021).
5. Ghoshhajra, R., Biswas, K. & Sarkar, A. A Review on Machine Learning Approaches for Predicting the Effect of Device Parameters on Performance of Nanoscale MOSFETs. in *2021 Devices for Integrated Circuit (DevIC)* 489–493 (2021). doi:10.1109/DevIC50843.2021.9455840.

6. Lennon, D. T. *et al.* Efficiently measuring a quantum device using machine learning. *Npj Quantum Inf.* **5**, 1–8 (2019).
7. Majeed, N. *et al.* Using Deep Machine Learning to Understand the Physical Performance Bottlenecks in Novel Thin-Film Solar Cells. *Adv. Funct. Mater.* **30**, 1907259 (2020).
8. Gambuzza, L. V. *et al.* A data driven model of TiO<sub>2</sub> printed memristors. in *2013 8th International Conference on Electrical and Electronics Engineering (ELECO)* 1–4 (2013).  
doi:10.1109/ELECO.2013.6713923.
9. Messaris, I. *et al.* A Data-Driven Verilog-A ReRAM Model. *IEEE Trans. Comput.-Aided Des. Integr. Circuits Syst.* **37**, 3151–3162 (2018).
10. Aadithya, K. *et al.* Development, Demonstration, and Validation of Data-driven Compact Diode Models for Circuit Simulation and Analysis. Preprint at <https://doi.org/10.48550/arXiv.2001.01699> (2020).
11. Liu, Y. *et al.* Machine Learning for Perovskite Solar Cells and Component Materials: Key Technologies and Prospects. *Adv. Funct. Mater.* **33**, 2214271 (2023).
12. Direct Growth of Aligned Zinc Oxide Nanorods on Paper Substrates for Low-Cost Flexible Electronics - Manekkathodi - 2010 - Advanced Materials - Wiley Online Library.  
<https://onlinelibrary.wiley.com/doi/epdf/10.1002/adma.201001289>.
13. Tin Oxide Nanorod Array-Based Photonic Memristors with Multilevel Resistance States Driven by Optoelectronic Stimuli | ACS Applied Materials & Interfaces.  
<https://pubs.acs.org/doi/full/10.1021/acsami.2c22362>.
14. Hydrothermally Grown TiO<sub>2</sub> Nanorod Array Memristors with Volatile States | ACS Applied Materials & Interfaces. <https://pubs.acs.org/doi/full/10.1021/acsami.0c05164>.
15. Jaafar, A. H. *et al.* Polymer/TiO<sub>2</sub> Nanorod Nanocomposite Optical Memristor Device. *J. Phys. Chem. C* **125**, 14965–14973 (2021).
16. Gao, S., Wang, Y., Wang, R. & Wu, W. Piezotronic effect in 1D van der Waals solid of elemental tellurium nanobelt for smart adaptive electronics. *Semicond. Sci. Technol.* **32**, 104004 (2017).
17. Hu, L. *et al.* An Optimized Ultraviolet-A Light Photodetector with Wide-Range Photoresponse Based on ZnS/ZnO Biaxial Nanobelt. *Adv. Mater.* **24**, 2305–2309 (2012).
18. Xiao, M. *et al.* Threshold Switching in Single Metal-Oxide Nanobelt Devices Emulating an Artificial



- Nociceptor. *Adv. Electron. Mater.* **6**, 1900595 (2020).
19. Ji, X. *et al.* TSSM: Three-State Switchable Memristor Model Based on Ag/TiO<sub>x</sub> Nanobelt/Ti Configuration. *Int. J. Bifurc. Chaos* **31**, 2130020 (2021).
  20. Sahatiya, P. & Badhulika, S. UV/ozone assisted local graphene (p)/ZnO(n) heterojunctions as a nanodiode rectifier. *J. Phys. Appl. Phys.* **49**, 265101 (2016).
  21. Zhang, C. *et al.* Nanofiber Architecture Engineering Implemented by Electrophoretic-Induced Self-Assembly Deposition Technology for Flash-Type Memristors. *ACS Appl. Mater. Interfaces* **14**, 3111–3120 (2022).
  22. Vasisth, S. E., Kotlarz, P. L., Gager, E. J. & Nino, J. C. 11 - Memristive applications of metal oxide nanofibers. in *Metal Oxide-Based Nanofibers and Their Applications* (eds. Esposito, V. & Marani, D.) 247–275 (Elsevier, 2022). doi:10.1016/B978-0-12-820629-4.00018-7.
  23. Tan, D., Jiang, C., Li, Q., Bi, S. & Song, J. Silver nanowire networks with preparations and applications: a review. *J. Mater. Sci. Mater. Electron.* **31**, 15669–15696 (2020).
  24. Milano, G., Porro, S., Valov, I. & Ricciardi, C. Recent Developments and Perspectives for Memristive Devices Based on Metal Oxide Nanowires. *Adv. Electron. Mater.* **5**, 1800909 (2019).
  25. Plasmonic-Radiation-Enhanced Metal Oxide Nanowire Heterojunctions for Controllable Multilevel Memory - Lin - 2016 - Advanced Functional Materials - Wiley Online Library.  
<https://onlinelibrary.wiley.com/doi/abs/10.1002/adfm.201601143>.
  26. Nagashima, K. *et al.* Switching Properties of Titanium Dioxide Nanowire Memristor. *Jpn. J. Appl. Phys.* **51**, 11PE09 (2012).
  27. Liang, K.-D. *et al.* Single CuO<sub>x</sub> Nanowire Memristor: Forming-Free Resistive Switching Behavior. *ACS Appl. Mater. Interfaces* **6**, 16537–16544 (2014).
  28. Opto-electronic memristors: Prospects and challenges in neuromorphic computing: Applied Physics Letters: Vol 117, No 23. <https://aip.scitation.org/doi/full/10.1063/5.0028539>.
  29. Yan, X. *et al.* Memristor with Ag-Cluster-Doped TiO<sub>2</sub> Films as Artificial Synapse for Neuroinspired Computing. *Adv. Funct. Mater.* **28**, 1705320 (2018).
  30. Huang, C.-H., Chang, H., Yang, T.-Y., Wang, Y.-C. & Chueh, Y.-L. Artificial Synapse Based on 2D-SnO<sub>2</sub> Memtransistor with Dynamically Tunable Analog Switching for Neuromorphic Computing. **31**.

31. Song, X., Qi, Q., Zhang, T. & Wang, C. A humidity sensor based on KCl-doped SnO<sub>2</sub> nanofibers. *Sens. Actuators B-Chem. - Sens. ACTUATOR B-CHEM* **138**, 368–373 (2009).
32. Liu, G. *et al.* Recent Advances in Resistive Switching Materials and Devices: From Memories to Memristors. *Eng. Sci.* **Volume 4 (December 2018)**, 4–43 (2018).
33. Poon, C.-T., Wu, D. & Yam, V. W.-W. Boron(III)-Containing Donor–Acceptor Compound with Goldlike Reflective Behavior for Organic Resistive Memory Devices. *Angew. Chem. Int. Ed.* **55**, 3647–3651 (2016).
34. Wang, R. *et al.* Recent Advances of Volatile Memristors: Devices, Mechanisms, and Applications. *Adv. Intell. Syst.* **2**, 2000055 (2020).
35. Yin, Y. *et al.* Hierarchical Hollow-Pore Nanostructure Bilayer Heterojunction Comprising Conjugated Polymers for High-Performance Flash Memory. *ACS Appl. Mater. Interfaces* **12**, 1103–1109 (2020).
36. Lv, J. *et al.* Structural and Carbonized Design of 1D FeNi/C Nanofibers with Conductive Network to Optimize Electromagnetic Parameters and Absorption Abilities. *ACS Sustain. Chem. Eng.* **6**, 7239–7249 (2018).
37. XPS and UPS Characterization of a Hybrid PbBr Perovskite Material with Work Function Measurement | Kratos. <https://www.kratos.com/application-areas/application-downloads/xps-and-ups-characterization-hybrid-pbbr-perovskite-material>.
38. Magari, Y., Makino, H., Hashimoto, S. & Furuta, M. Origin of work function engineering of silver oxide for an In–Ga–Zn–O Schottky diode. *Appl. Surf. Sci.* **512**, 144519 (2020).
39. Nb<sub>2</sub>O<sub>5</sub> nanofiber memristor: Applied Physics Letters: Vol 103, No 5. <https://aip.scitation.org/doi/10.1063/1.4817302>.
40. Belov, A. N. Resistive switching of CuO nanofibers embedded into hollow channels of SiO<sub>2</sub> layer. doi:10.1088/1742-6596/1400/5/055006.
41. Patil, A. A., Wagh, S. V., Dongale, T. D. & Kim, D. Electrospun 1D f-MWCNTs–TiO<sub>2</sub> composite nanofibers for resistive memory and synaptic learning applications. *Mater. Lett.* **280**, 128587 (2020).
42. Rong, H. *et al.* Demonstration of electronic synapses using a sericin-based bio-memristor. *Appl. Phys. Express* **16**, 031007 (2023).
43. Ultrasensitive gas sensor developed from SnS/TiO<sub>2</sub>-based memristor for dilute methanol detection at

room temperature. *Sens. Actuators B Chem.* **392**, 134038 (2023).

Journal Pre-proof

**Declaration of interests**

☒ The authors declare that they have no known competing financial interests or personal relationships that could have appeared to influence the work reported in this paper.

☐ The authors declare the following financial interests/personal relationships which may be considered as potential competing interests:

--